



## OPTICS

# Ultralow voltage–driven efficient and stable perovskite light-emitting diodes

Song Zheng<sup>1</sup>, Zhibin Wang<sup>1\*</sup>, Naizhong Jiang<sup>1</sup>, Hailiang Huang<sup>1</sup>, Ximing Wu<sup>1</sup>, Dan Li<sup>1</sup>, Qian Teng<sup>2</sup>, Jinyang Li<sup>2</sup>, Chenhao Li<sup>2</sup>, Jinsui Li<sup>2</sup>, Tao Pang<sup>3</sup>, Lingwei Zeng<sup>4</sup>, Ruidan Zhang<sup>1</sup>, Feng Huang<sup>1</sup>, Lei Lei<sup>5</sup>, Tianmin Wu<sup>6</sup>, Fanglong Yuan<sup>2\*</sup>, Daqin Chen<sup>1,7,8\*</sup>

The poor operational stability of perovskite light-emitting diodes (PeLEDs) remains a major obstacle to their commercial application. Achieving high brightness and quantum efficiency at low driving voltages, thus effectively reducing heat accumulation, is key to enhancing the operational lifetime of PeLEDs. Here, we present a breakthrough, attaining a record-low driving voltage while maintaining high brightness and efficiency. By thoroughly suppressing interface recombination and ensuring excellent charge transport, our PeLEDs, with an emission peak at 515 nanometers, achieve a maximum brightness of 90,295 candelas per square meter and a peak external quantum efficiency of 27.8% with an ultralow turn-on voltage of 1.7 volts (~70% bandgap voltage). Notably, Joule heat is nearly negligible at these low driving voltages, substantially extending the operational lifetime to 7691.1 hours. Our optimized strategies effectively tackle stability issue through thermal management, paving the way for highly stable PeLEDs.

## INTRODUCTION

Metal halide perovskite light-emitting diodes (PeLEDs) are increasingly recognized as a new-generation candidate for efficient, low-cost, and vivid displays due to their outstanding optical and electrical properties (1–6). Current state-of-the-art PeLEDs achieve external quantum efficiencies (EQEs) of 26.1% for red, 30.8% for green, and 21.4% for blue emitters (7–9). However, their high turn-on voltage ( $V_T$ , defined as  $1 \text{ cd m}^{-2}$ ) limits the brightness and EQE at low driving voltages, lagging behind commercial LEDs based on III-V semiconductors (10). Electroluminescence (EL) at subbandgap voltages, observed in various emitter systems, including inorganic semiconductors (10), organic LEDs (11), quantum dot LEDs (QLEDs) (12), and PeLEDs (13), offers a potential solution. Operating below the bandgap voltage—defined as the optical bandgap ( $E_g$ ) of the emissive layer divided by the elementary charge ( $q$ )—requires additional thermal energy for electron transition to higher energy states, leading to photon emission (14–16). Hence, lowering the driving voltage below the subbandgap level reduces Joule heat generation, addressing stability issues, and mitigates electric field–induced ion migration within the perovskite emitter, thereby enhancing device longevity (17).

Zhao *et al.* (18–19) identified Joule heating as a critical factor in the rapid degradation of PeLEDs and suggested thermal management

strategies to enhance device stability. However, few studies have focused on directly reducing intrinsic Joule heat within the device (20). Recently, Gao *et al.* (14) achieved a high brightness of  $1100 \text{ cd m}^{-2}$  and an EQE of 23% at bandgap voltage in red QLEDs. Because of the minimized heat generation achieved by reducing the driving voltage, the  $T_{95}$  lifetime (the time for the luminance to decrease to 95% of the initial value) was improved to 48,000 hours. This study has inspired us to reconsider heat management in PeLEDs, with a particular focus on the influence of driving voltage. Unfortunately, despite reports of subbandgap driving PeLEDs in various architectures, achieving high device performance at low voltages is yet to be demonstrated (Table 1). This challenge stems from two primary factors: First, achieving a high quantum yield in perovskite emitters frequently necessitates compromising on charge transport ability, resulting in reduced charge transport efficiency; second, the inadequate conductivity of the charge transport layers hinders subbandgap emission, while interfacial luminescent quenching further exacerbates the loss of brightness and efficiency (10). To achieve high-performance light emission at low voltages, it is crucial to suppress interface recombination at the junctions between perovskite grains and emitter/charge transfer layers (CTLs) while ensuring efficient charge transport throughout the device.

In this study, we have successfully achieved high-brightness green PeLEDs with a record-breaking ultralow  $V_T$  of 1.7 V by optimizing both the emitter and adjacent CTLs. We develop a three-dimensional (3D)/0D heterostructure emitter by embedding CsPbBr<sub>3</sub> nanocrystals (NCs) into 0D Cs<sub>4</sub>PbBr<sub>6</sub>, resulting in near-unity photoluminescence quantum yield (PLQY) and rapid radiative recombination. Complementing the emitter, we have redesigned the electron and hole transport layers (HTLs) to optimize charge carrier injection, exciton confinement, and interfacial defect passivation. This leads to a subbandgap emissive PeLED with a high EQE of 27.8%, a brightness of 90,295  $\text{cd m}^{-2}$ , and an ultranarrow emission bandwidth of 18 nm. Moreover, the resulting PeLED exhibits high efficiency (>20%) over a broad brightness range (500 to 25,000  $\text{cd m}^{-2}$ ) at low driving voltages (2.2 to 2.7 V). The substantial reduction in driving voltage effectively minimizes heat generation within the device, consequently

<sup>1</sup>College of Physics and Energy, Fujian Normal University, Fujian Provincial Key Laboratory of Quantum Manipulation and New Energy Materials, Fuzhou 350117, China.

<sup>2</sup>Key Laboratory of Theoretical and Computational Photochemistry of Ministry of Education, College of Chemistry, Beijing Normal University, Beijing 100875, China.

<sup>3</sup>Huzhou Key Laboratory of Materials for Energy Conversion and Storage, College of Science, Huzhou University, Huzhou 313000, China.

<sup>4</sup>School of Chemistry and Chemical Engineering, Hunan University of Science and Technology, Xiangtan, Hunan 411201, China.

<sup>5</sup>Institute of Optoelectronic Materials and Devices, China Jilijian University, Hangzhou 310018, China.

<sup>6</sup>Key Laboratory of Opto-Electronic Science and Technology for Medicine of Ministry of Education, College of Photonic and Electronic Engineering, Fujian Normal University, Fuzhou 350117, China.

<sup>7</sup>Fujian Provincial Collaborative Innovation Center for Advanced High-Field Superconducting Materials and Engineering, Fuzhou 350117, China.

<sup>8</sup>Fujian Provincial Engineering Technology Research Center of Solar Energy Conversion and Energy Storage, Fuzhou 350117, China.

\*Corresponding author. Email: zhibinwang@fjnu.edu.cn (Z.W.); flyuan@bnu.edu.cn (F.Y.); dqchen@fjnu.edu.cn (D.C.)

**Table 1. Summary of key device parameters of the green PeLEDs.** *L*, luminance;  $V_T$ , turn-on voltage. The brightness and partial  $V_T$  values of PeLEDs were estimated from the figure in references.

Perovskites	$V_T$ (V)	Voltage at 1000 cd m <sup>-2</sup> (V)	<i>L</i> at bandgap (cd m <sup>-2</sup> )	<i>L</i> at 2.6 V (cd m <sup>-2</sup> )	Reference
Quasi-core/shell	2.7	3.3	<1	<1	(4)
Quasi-2D	2.8	4.1	<1	<1	(5)
Quasi-2D	~3.0	3.8	<1	<1	(21)
In situ core/shell NCs	2.22	2.6	<100	~3000	(38)
QD solids	~2.9	3.5	<1	<1	(24)
Quasi-2D	3.0	4.8	<1	<1	(8)
Quantum wires	4.8	6.8	<1	<1	(6)
Quasi-2D	2.1	3.0	<100	~300	(42)
3D/0D core/shell NCs	1.7	2.3	2248	9842	This work

greatly extending the operational lifetime to 7691.1 hours at 100 cd m<sup>-2</sup>. Our optimized strategies effectively address the stability challenges in perovskite devices, paving the way for the development of highly efficient and stable PeLEDs.

## RESULTS

### Self-assembly 3D/0D heterostructure emitter

For achieving high device performance, a crucial prerequisite is a high-quality emitter that necessitates a harmonious blend of factors, including exceptional luminescent efficiency, minimal trap density, and efficient charge transport. The PLQY of 3D perovskite is greatly affected by defects because of their weak exciton binding energies ( $E_b$ ) and low radiative recombination rates (fig. S1A). Current methods often enhance exciton confinement by adding bulky organic cations to form quasi-2D structures, thereby increasing PLQY (21, 22). However, this approach introduces low-*n* phases that cause additional defects and impair charge transport (fig. S1B). Cs<sub>4</sub>PbBr<sub>6</sub>, as a wide bandgap 0D perovskite derivative, has attracted attention for its elemental compatibility and lattice matching, which aid in passivation and stabilization of perovskite crystals (fig. S1C) (23). Because of the competitive formation mechanisms among 3D, quasi-2D, and 0D phases during the in situ growth process on substrate, precise regulation of the perovskite precursor is essential for effective defect suppression while maintaining excellent charge transport performance. To this end, we designed a precursor solution with formamidinium bromide (FABr), phenylethyl ammonium bromide (PEABr), cesium bromide (CsBr), and lead bromide (PbBr<sub>2</sub>) in a molar ratio of *x*:0.35:1:1, where “*x*” represents the molar ratio of FABr to PbBr<sub>2</sub>. The resulting perovskite films, labeled as “*x*-FABr films” were analyzed using x-ray diffraction (XRD). The 0-FABr film exhibits diffraction peaks at 15.2°, 21.6°, and 30.7°, corresponding to nanometer-sized CsPbBr<sub>3</sub> crystals with an average diameter of 8.8 nm (Fig. 1A) (24). Grazing-incidence wide-angle x-ray scattering (GIWAXS) patterns reveal broad and uniform Debye-Scherrer rings at  $q = 1.07, 1.51, \text{ and } 2.14 \text{ \AA}^{-1}$ , corresponding to the (100), (110), and (200) planes of CsPbBr<sub>3</sub>, clearly depicting the formation of in situ self-assembly perovskite NCs with random crystalline orientation (Fig. 1B).

Upon increasing *x* from 0 to 0.2, three new characteristic peaks emerged in the XRD pattern (Fig. 1A). To identify the new peaks,

we deposited the 0.2-FABr sample on a zero-background holder (single crystal silicon). The diffraction peaks matched well with the standard diffraction patterns of Cs<sub>4</sub>PbBr<sub>6</sub> and CsPbBr<sub>3</sub>, indicating the coexistence of both 0D and 3D phases in the 0.2-FABr sample (fig. S2) (23, 25). GIWAXS patterns also confirmed the 0D phase, revealing two scattering rings at  $q = 0.91 \text{ and } 2.04 \text{ \AA}^{-1}$ , suggesting a random distribution of Cs<sub>4</sub>PbBr<sub>6</sub> orientation (Fig. 1C). In prior studies, the formation of Cs<sub>4</sub>PbBr<sub>6</sub> was typically achieved using an excess of CsBr. However, this required substantially more CsBr than PbBr<sub>2</sub>, posing challenges for charge injection in PeLEDs (26). By using alternative perovskite-related additives, such as FABr and KBr, the 0D phase can be achieved with a minimal addition, which has been proved by other research groups (25, 27, 28). In our case, it is evident that even at low doses of *x* = 0.2, the successful induction of 0D Cs<sub>4</sub>PbBr<sub>6</sub> can be observed. In contrast, no 0D phases appeared in the XRD pattern when the same ratio of CsBr or MABr was added, indicating that FABr is more effectively to promote the formation of 0D phase (fig. S3).

The incorporation of bulky PEABr in the perovskite precursor may also influence the formation of the 0D phase. To verify this hypothesis, we removed PEABr from the precursor and examined the effect of various ABr<sub>s</sub> (A: FA<sup>+</sup>, MA<sup>+</sup>, and Cs<sup>+</sup>) on the 0D phase. In the absence of PEABr (fig. S4), a higher amount of AX was required to obtain the 0D phase, suggesting that both PEABr and FABr in the optimized precursor promote 0D phase formation. Although PEABr has been reported to introduce Ruddlesden-Popper (RP) layered perovskites, in our case, PEABr functions primarily as a passivator. Its absence markedly affects the PLQY of the films (fig. S5). Because of the low concentration of PEABr and the inclusion of crown ethers to inhibit the RP phase, no layered perovskite signal was detected in the XRD patterns, supporting our inference. The absorption spectra of perovskite films with and without PEABr indicated that the primary absorption peaks stem from 3D and 0D perovskites (fig. S6), consistent with the XRD results.

However, the microphysical mechanism behind the FABr-promoted formation of the 0D phase requires further investigation. Figure 1D illustrates the reaction kinetics of 0D Cs<sub>4</sub>PbBr<sub>6</sub> synthesis with FABr assistance, as revealed by first-principles calculations. In a perovskite precursor solution containing FABr, CsBr, and PbBr<sub>2</sub>, four potential reaction pathways for Cs<sub>4</sub>PbBr<sub>6</sub> formation are identified. In path I (blue line), without FABr, CsBr and PbBr<sub>2</sub> directly

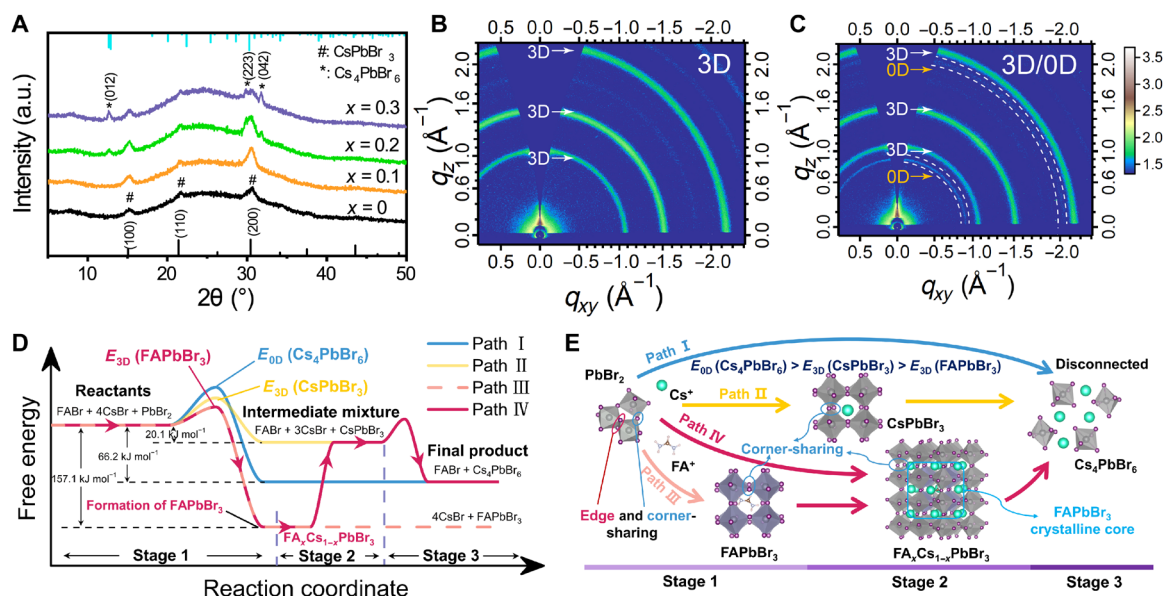


**Fig. 1. The crystallographic characterization and reaction kinetics of 3D/0D heterostructure.** (A) XRD patterns of  $x$ -FABr films ( $x = 0$  to  $0.3$ ). GIWAXS patterns of (B) 3D  $\text{CsPbBr}_3$  and (C)  $\text{CsPbBr}_3/\text{Cs}_4\text{PbBr}_6$ . (D) A schematic reaction kinetics diagram of four competing paths (paths I to IV) in the FABr-assisted synthesis of 0D  $\text{Cs}_4\text{PbBr}_6$  from the precursors. (E) Microstructural diagram of various pathways in the FABr-assisted synthesis of 0D  $\text{Cs}_4\text{PbBr}_6$ . a.u., arbitrary units.

react to form  $\text{Cs}_4\text{PbBr}_6$  with an activation energy of  $E_{0D}$  ( $\text{Cs}_4\text{PbBr}_6$ ). In path II (yellow line), also without FABr,  $\text{CsBr}$  and  $\text{PbBr}_2$  first generate a  $\text{CsPbBr}_3$  intermediate with an activation energy of  $E_{3D}$  ( $\text{CsPbBr}_3$ ), which then reacts with additional  $\text{CsBr}$  to produce  $\text{Cs}_4\text{PbBr}_6$ . In path III (pink line), a small amount of FABr reacts with  $\text{PbBr}_2$  forming  $\text{FAPbBr}_3$  with an activation energy of  $E_{3D}$  ( $\text{FAPbBr}_3$ ). In path IV (red line), the  $\text{FAPbBr}_3$  formed in path III acts as a crystalline nucleus, promoting the formation of a  $\text{FA}_x\text{Cs}_{1-x}\text{PbBr}_3$  intermediate, which then reacts with remaining  $\text{CsBr}$  to ultimately yield  $\text{Cs}_4\text{PbBr}_6$ . The competition among different reaction pathways indicates that the relative kinetics of the four pathways are crucial in determining the dominant reaction pathway (29). Since the formation of 3D  $\text{FAPbBr}_3$  has the lowest activation energy of  $-157.1 \text{ kJ mol}^{-1}$  [ $E_{0D}$  ( $\text{Cs}_4\text{PbBr}_6$ ) >  $E_{3D}$  ( $\text{CsPbBr}_3$ ) >  $E_{3D}$  ( $\text{FAPbBr}_3$ )], path IV is expected to be the reaction (30–32). The low activation energy favors the rapid formation of  $\text{FAPbBr}_3$  (stage 1; Fig. 1E), which acts as a crystalline nucleus, promoting the growth of  $\text{CsPbBr}_3$  (or  $\text{FA}_x\text{Cs}_{1-x}\text{PbBr}_3$ ) in stage 2. In stage 3, a structural rearrangement from corner-sharing  $[\text{PbBr}_6]^{4-}$  octahedra ( $\text{FA}_x\text{Cs}_{1-x}\text{PbBr}_3$ ) to isolated  $[\text{PbBr}_6]^{4-}$  octahedra in  $\text{Cs}_4\text{PbBr}_6$  occurs, resulting in the “3D-embedded 0D” configuration.

The morphologies of perovskite films were characterized using a scanning electron microscope (SEM). As shown in Fig. 2A, the 0-FABr film features numerous small grains around 10 nm. While these small grains contribute to good charge carrier confinement, the abundant grain boundaries can still harbor numerous nonradiative recombination defects. In contrast, the 0.2-FABr film has a more compact morphology with no obvious grains or pinholes (Fig. 2B). Atomic force microscopy further revealed that incorporating FABr reduced the root mean square roughness from 2.82 to 1.29 nm (fig. S7). The emitter thickness was estimated to be 47 nm from the cross-sectional SEM image (fig. S8). Transmission electron microscopy (TEM) was used to further characterize the perovskite morphology. The emitter layer was peeling off the substrate into a chlorobenzene (CB) solution and deposited onto a copper mesh for

observation (33). The perovskite NCs for 0-FABr sample are homogeneous spherical particles with an average size of 10.8 nm (Fig. 2C and fig. S9), consistent with the XRD and SEM results. High-resolution TEM (HRTEM) image and selected area fast Fourier transformation analysis identified two intersecting lattice planes at 3.0 and 2.1 Å, corresponding to the (200) and (022) planes of  $\text{CsPbBr}_3$ . In the 0.2-FABr sample, HRTEM reveals two distinct lattice fringes (Fig. 2D). The pink box shows fringes corresponding to the (104) and (223) planes of  $\text{Cs}_4\text{PbBr}_6$ , while the cyan box displays fringes corresponding to the (200) and (110) planes of  $\text{CsPbBr}_3$ . This offers direct evidence for the existence of  $\text{CsPbBr}_3$  embedded in  $\text{Cs}_4\text{PbBr}_6$ , forming a 3D/0D heterostructure. Additional HRTEM images confirm the substantial evolution induced by FABr, leading to the formation of the unique 3D/0D core/shell NC structure (fig. S10).

Time-of-flight secondary ion mass spectrometry (ToF-SIMS) and x-ray photoelectron spectroscopy depth analysis were performed to investigate the vertical distribution of  $\text{PEABr}$ , FABr, and the 0D phase. We observed a rapid attenuation of the  $\text{PEA}^+$  signal with increasing the probing depth, indicating that  $\text{PEA}^+$  is primarily distributed at the top of the emitter, acting as a passivator to suppress the nonradiative recombination (fig. S11, A and B). With the addition of FABr, signals belonging to  $\text{FA}^+$  appeared, along with a characteristic signal of the 0D phase (fig. S11, C and D).  $\text{FA}^+$ , similar to  $\text{PEA}^+$ , is primarily distributed at the upper interface of the emitter, whereas the 0D perovskite is distributed throughout the entire thin film.

### Enhancement of optoelectronic properties via a 3D/0D heterostructure

The optical and electrical properties of perovskite films with various FABrs were investigated to explore their potential for PeLEDs. The 0.2-FABr sample achieved a near unity of PLQY (96%), remarkably higher than the pristine sample (58%) (Fig. 3A), demonstrating the excellent passivation effect of  $\text{Cs}_4\text{PbBr}_6$ . Furthermore, the full width

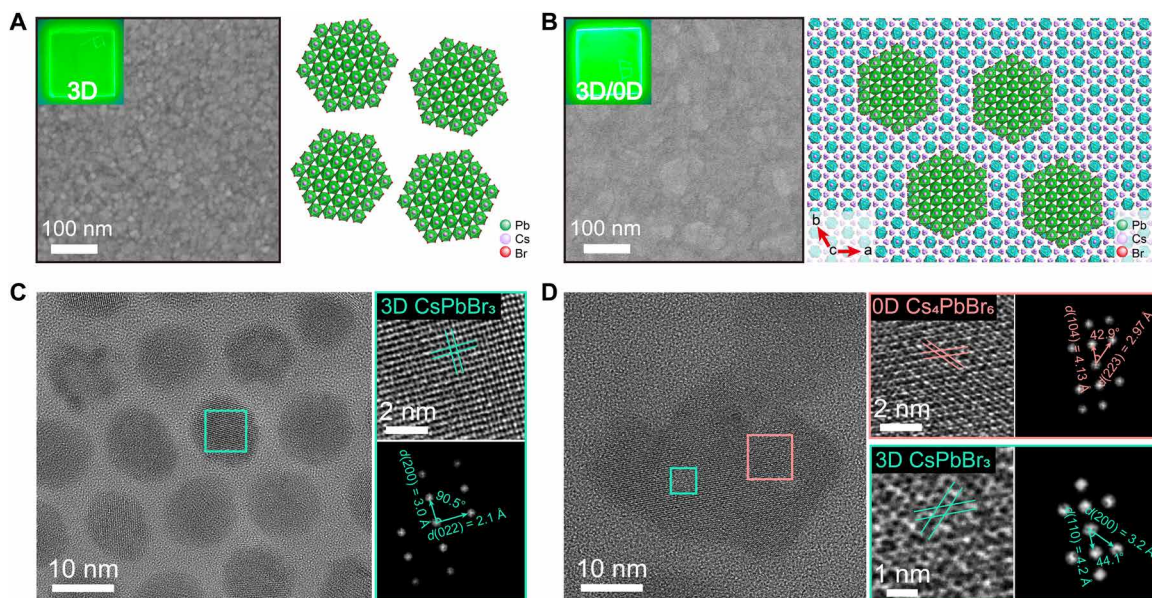


**Fig. 2. The morphological characterization of 3D/0D heterostructure.** SEM images of  $x$ -FABr films with (A)  $x = 0$  and (B)  $x = 0.2$ . Insets are corresponding photographs of pure  $\text{CsPbBr}_3$  NCs and  $\text{CsPbBr}_3$ & $\text{Cs}_4\text{PbBr}_6$  heterostructure films under ultraviolet (UV) light. HRTEM images of  $x$ -FABr films with (C)  $x = 0$  and (D)  $x = 0.2$ , with cyan boxes indicating 3D  $\text{CsPbBr}_3$  and pink box representing 0D  $\text{Cs}_4\text{PbBr}_6$ . Fast Fourier transformation images were obtained from magnified HRTEM images.

at half maximum (FWHM) in photoluminescence (PL) spectra narrowed from 22.5 to 18.2 nm as the FABr increased from 0 to 0.3 (Fig. 3B). Notably, the FWHM of our optimized samples is considerably narrower compared to traditional quasi-2D perovskites, which typically exceed 20 nm and can reach up to 30 nm due to incomplete energy transfer and defect-rich low- $n$  phases (8, 34). In contrast, introducing 0D  $\text{Cs}_4\text{PbBr}_6$  into 3D perovskite preserves high color purity due to a more rational energy level structure (21, 22, 25).

Carrier recombination dynamics were determined using time-resolved PL spectra (fig. S12 and table S1). The average decay lifetime ( $\tau_{\text{ave}}$ ) substantially reduces from 761 to 62 ns with an increased ratio of FABr to 0.2. A higher PLQY and a shorter PL lifetime suggest more efficient radiative recombination. At  $x = 0.2$ , the radiative recombination rate reached  $15.7 \mu\text{s}^{-1}$ , which is 20 times higher than the pristine sample (Fig. 3C). Note that high PLQY value and fast radiative recombination rate are beneficial for enhancing the emission intensity of PeLED at low driving voltages (14).

To gain more insights into the influence of 0D  $\text{Cs}_4\text{PbBr}_6$  on the optical properties of  $\text{CsPbBr}_3$  NCs, we recorded temperature-dependent PL spectra of 3D and 3D/0D perovskite samples (Fig. 3D). In the 3D perovskite, a decrease in temperature revealed an additional broad subbandgap emission that was red-shifted with respect to the band-edge emission peak. This additional broad subbandgap emission can be attributed to the radiative recombination of trapped excitons caused by the presence of numerous defect traps at grain surface (35–37). Conversely, the 3D/0D perovskite sample exhibited a narrow single peak, indicating effective passivation of defect traps upon the introduction of the 0D phase. Besides, the  $E_b$  value increases from 130.5 to 151.1 eV after the formation of 3D/0D heterostructure, suggesting enhanced exciton confinement due to the formation of type-I band alignment.

Carrier mobilities of  $x$ -FABr films were then extracted using space charge-limited current measurements (Fig. 3E and fig. S13). As  $x$

increases from 0 to 0.2, hole mobility exhibits a nearly one-order-of-magnitude increase, rising from  $7.80 \times 10^{-3}$  to  $7.69 \times 10^{-2} \text{ cm}^2 \text{ V}^{-1} \text{ s}^{-1}$ . Furthermore, the electron mobility of 0.2-FABr film increases approximately threefold, reaching  $2.91 \times 10^{-2} \text{ cm}^2 \text{ V}^{-1} \text{ s}^{-1}$ . The optimized sample exhibited a substantial increase in carrier mobilities, comparable to previous reported results (38, 39). Enhanced mobilities for both holes and electrons improve charge injection and transport, leading to increased brightness and reduced  $V_T$ .

### Designing the architecture for subbandgap emissive PeLEDs

To achieve high brightness and efficiency at low driving voltages, redesigning CTLs to enhance electrical conductivity and improve interfacial passivation is necessary. Recent advances in HTLs using phosphonic acid group-anchored carbazole-based self-assembled monolayers have shown notable promise in perovskite solar cells and PeLEDs (40–42). Here, we addressed the hydrophobic nature of [4-(3,6-dimethyl-9H-carbazol-9-yl)butyl]phosphonic acid (Me-4PACz) by incorporating the highly hydrophilic polyvinyl pyrrolidone (PVP). As depicted in Fig. 4A, poly-TPD  $\{[N,N'$ -bis(4-butylphenyl)- $N,N'$ -bis(phenyl)benzidine] $\}$  was deposited on indium tin oxide (ITO) as hole injection layer owing to its high hole mobility. In addition, Me-4PACz:PVP served as an interfacial modified layer. The blending of Me-4PACz with PVP markedly decreases the water contact angle from  $56.3^\circ$  to  $33.1^\circ$ , creating a more hydrophilic interface (Fig. 4B).

It is well known that perovskite films deposited on traditional HTLs such as PEDOT:PSS,  $\text{NiO}_x$ , poly(9-vinylcarbazole), etc., suffer from varying degrees of PL quenching (42–44). To investigate the PL quenching effect on various substrates, we performed the measurements of PL spectra. Compared to perovskite films deposited on nonconductive quartz, those on PEDOT:PSS-coated substrates show notable PL quenching (fig. S14). Perovskite film on Me-4PACz:PVP-coated substrates exhibits higher PL intensity than those on quartz,

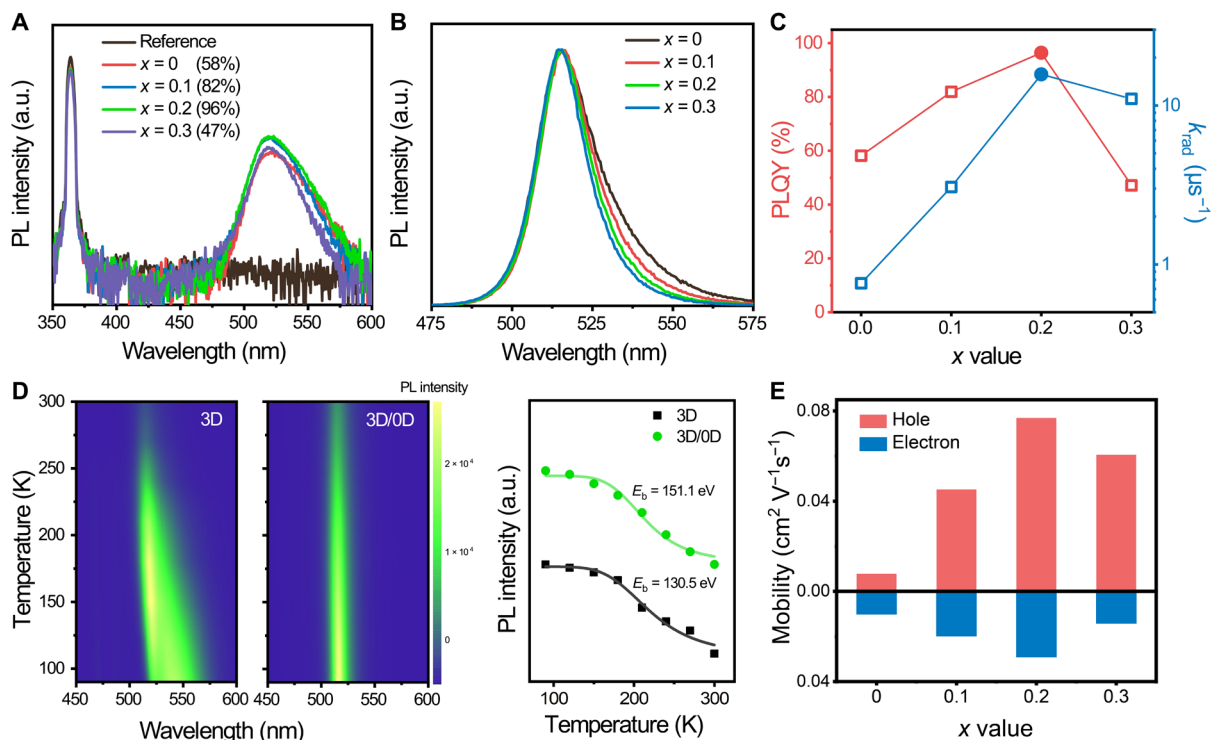


**Fig. 3. Optical and electrical characterization of perovskite films.** (A) PLQY spectra, (B) normalized PL spectra, (C) PLQY values, and radiative recombination rates of *x*-FABr films (*x* = 0 to 0.3). (D) Temperature-dependent PL spectra and estimated  $E_b$  values of 3D and 3D/OD perovskites. (E) Hole and electron mobilities of *x*-FABr films (*x* = 0 to 0.3).

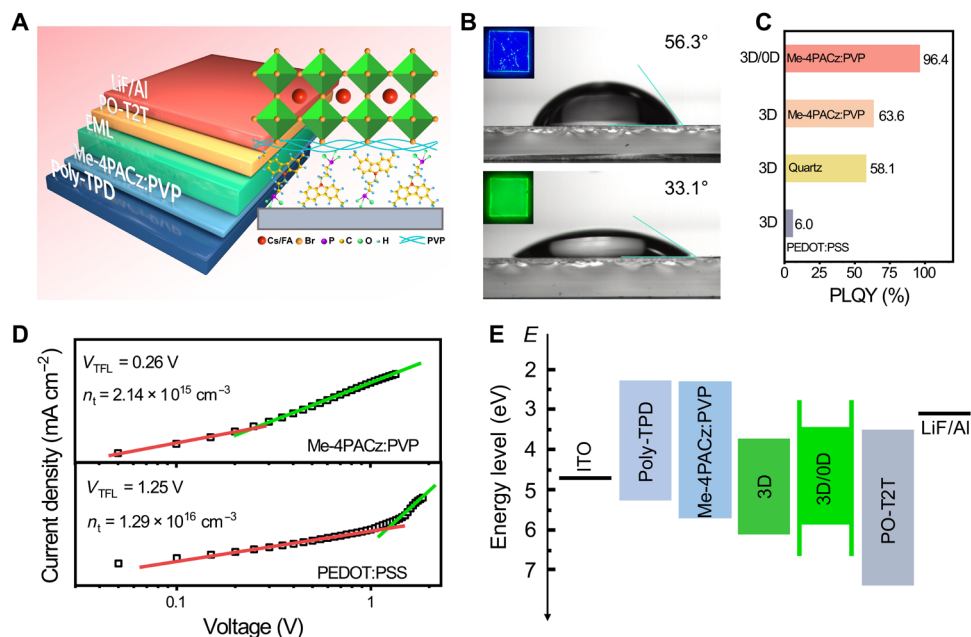


**Fig. 4. Collaborative optimization of the HTL and ETL.** (A) Schematic diagram of the PeLED device architecture. (B) Contact angle measurements of Me-4PACz and Me-4PACz:PVP films. (C) PLQY values of perovskite thin films deposited on various substrates (PEDOT:PSS, glass, and poly-TPD/Me-4PACz:PVP). (D) The corresponding *J-V* curves of hole-only devices with various HTLs. (E) Schematic diagram of the energy level alignment of subbandgap emissive PeLEDs.

likely due to the passivation effect of phosphonic acid in Me-4PACz. Similar results were observed in the absolute PLQY measurements (Fig. 4C), with PLQY increasing from 6.0% to 58.1% and further to 63.6% upon replacing PEDOT:PSS with quartz and subsequently with Me-4PACz:PVP. Moreover, a near-unity PLQY was achieved in a 3D/0D emitter deposited on the Me-4PACz:PVP substrate, highlighting the exceptional luminescent performance resulting from collaborative optimization from the emitter to the buried interface. To verify this, hole-only devices with emitter deposited on PEDOT:PSS or poly-TPD/Me-4PACz:PVP were fabricated to investigate the charge carrier properties using the space charge-limited current method. The trap-filled limited voltage ( $V_{TFL}$ ) decreased from 1.25 to 0.26 V after the use of Me-4PACz:PVP-modified layer, corresponding to a notable reduction of trap-state density from  $1.29 \times 10^{16}$  to  $2.14 \times 10^{15} \text{ cm}^{-3}$  (Fig. 4D). The reduction in trap-state density further confirmed the effective defects suppression achieved by fabricating a 3D/0D heterostructure on the Me-4PACz:PVP-buried interface.

The impact of FABr on the electronic structure of the perovskite emitter was subsequently investigated using ultraviolet (UV) photoelectron spectroscopy (fig. S15). As the  $x$  increases from 0 to 0.2, both the work function and valence band maximum (VBM) shift to shallower levels, transitioning from 4.77 and  $-6.11 \text{ eV}$  to 4.58 and  $-5.83 \text{ eV}$ , respectively. This upshift can be attributed to the alleviation of the self-p-doping effect caused by ionic defects at the perovskite crystal interfaces (38). The upshifted VBM facilitates hole injection from the HTL to the emitter, creating a favorable bandgap alignment with HTL. After the PVP modification (fig. S16), the HOMO (highest occupied molecular orbital) of the Me-4PACz shifted from  $-5.44$  to  $-5.65 \text{ eV}$ , reducing the hole-injection barrier. As shown in Fig. 4E, the overall hole injection and transport abilities of the device were improved through the utilization of the Me-4PACz:PVP modifier and a FABr-doped emitter layer. To better maintain electron/hole injection balance, the conventional electron transport layer (ETL) TPBi was replaced by PO-T2T {2,4,6-tris[3-(diphenylphosphinyl)phenyl]-1,3,5-triazine}, which exhibits electron mobility two orders of magnitude higher ( $1.7 \times 10^{-3}$  to  $4.4 \times 10^{-3} \text{ cm}^2 \text{ V}^{-1} \text{ s}^{-1}$ ) than TPBi ( $3.3 \times 10^{-5} \text{ cm}^2 \text{ V}^{-1} \text{ s}^{-1}$ ). Moreover, the P=O functional groups in PO-T2T are conducive to top-surface passivation for perovskite films (45, 46). The device performance will be discussed later. The deep HOMO energy level ( $-7.39 \text{ eV}$ ) and the high triplet energy level (3.0 eV) of PO-T2T can efficiently block the energy transfer from emitter to ETL (46).

### Device performance of PeLEDs

We explored the device performance using the 3D/0D core/shell perovskite NCs emitter and optimized interfacial architecture. Specifically, we used a subbandgap emissive PeLED configuration consisting of ITO/poly-TPD/Me-4PACz:PVP/core-shell perovskite NCs/PO-T2T/LiF/Al (labeled as “device I”). For comparison, a conventional PeLED without subbandgap emission was fabricated, consisting of ITO/PEDOT:PSS/3D perovskite NCs/TPBi/LiF/Al (labeled as “device II”). The optimized device exhibited an ultralow subbandgap  $V_T$  of only 1.7 V (Fig. 5A), and in some instances, the  $V_T$  could reach as low as 1.5 V, as evidenced by the statistical data (fig. S17). We note that the origin of the low  $V_T$  is highly dependent on both the ETL and emitter. As depicted in fig. S18 (A and B), when using TPBi as the ETL, PeLEDs consistently demonstrate a relatively high  $V_T$  (2.8 V), regardless of the specific HTL used. Previous studies

indicate that PeLEDs exhibiting subbandgap luminescence typically incorporate ETLs characterized by high electron mobility, such as ZnO (47, 48). Thus, it can be inferred that the utilization of the high-electron mobility material, PO-T2T, in this study also profoundly contributes to subbandgap emission. Upon replacing TPBi with PO-T2T, the  $V_T$  decreased from 2.8 to 2.0 V due to the reduced electron injection barrier (fig. S18, C and D). Subsequently, the  $V_T$  further decreased to 1.7 V after using the core-shell perovskite emissive layer, possibly ascribed to the upshifted VBM and enhanced hole/electron mobilities of the emitter. The reduced  $V_T$  is also observed in devices using PEDOT:PSS as the HTL (fig. S19). As FABr increases, the  $V_T$  of PeLEDs progressively reduced, accompanied by sustained improvements in brightness and efficiency. Table S2 shows that using an ETL with high charge carrier mobility and a FABr-doped emissive layer is crucial for achieving subbandgap emission, as these factors substantially minimize parasitic series resistance.

The EL spectra of PeLEDs fabricated using the 3D CsPbBr<sub>3</sub> NCs and the 3D/0D core/shell perovskite NCs align with the corresponding PL spectra, all peaking at 515 nm (Fig. 5B). Similar to the PL spectra, the 3D/0D perovskite-based PeLED exhibits a purer emission with an FWHM of only 18.3 nm, noticeably narrower than the pristine sample (24.4 nm). Consequently, the PeLEDs achieved a maximum brightness of  $90,295 \text{ cd m}^{-2}$ , whereas the pristine PeLEDs displayed a maximum brightness of only  $14,820 \text{ cd m}^{-2}$ . Last, a maximum EQE of 27.8% was achieved at a high brightness of  $\sim 10,000 \text{ cd m}^{-2}$  (the precise value being  $9843 \text{ cd m}^{-2}$ ) and a low bias of only 2.6 V (Fig. 5C). The distribution of luminance and EQE from 20 devices demonstrates the good reproducibility of our optimized PeLEDs, with an average luminance of  $82,607 \text{ cd m}^{-2}$  and an average EQE of 23.3% (fig. S20). It should be emphasized that the ultralow driving voltage is remarkably lower than that of most state-of-the-art green PeLEDs; the majority of them cannot even turn on at such voltage. Furthermore, the optimized device sustained an EQE value exceeding 20% over a wide range of ultrahigh brightness levels, spanning from  $\sim 500$  to  $25,000 \text{ cd m}^{-2}$ , within a current density range of 1.5 to  $55 \text{ mA cm}^{-2}$ , and under a low driving voltage from 2.2 to 2.7 V, given the fact that practical outdoor display devices typically require a brightness exceeding  $5000 \text{ cd m}^{-2}$  (49–51). Our devices, delivering high brightness at a low driving voltage, provide a key reference for advancing the next generation of ultrahigh-resolution displays.

It is universally recognized that the driving voltage is intricately linked to the generation of Joule heat in a device and minimizing this heat is crucial for extending the operational lifetime. The correlation between driving voltage and heat generation was investigated using infrared thermography, with temperatures recorded after running for 5 min at various brightness levels. The PeLEDs with the optimized structure (device I) show negligible temperature increase, ranging from  $25.3^\circ$  to  $25.6^\circ\text{C}$ , as the brightness increases from 0 to  $10,000 \text{ cd m}^{-2}$  (Fig. 5D). In contrast, the control PeLEDs (device II) exhibit a noticeable temperature rise, ranging from  $25.0^\circ$  to  $83.7^\circ\text{C}$  under the same brightness levels. From the photographs of devices, the device I can maintain high brightness due to minimal thermal generation, while a substantial amount of Joule heat leads to a rapid decline in brightness of device II within a short period (5 min). The device operational stability was then assessed in a  $\text{N}_2$ -filled glove box (Fig. 5E). At an initial luminance of  $100 \text{ cd m}^{-2}$  ( $L_0$ ), the  $T_{50}$  lifetime of control PeLEDs (device II) was directly measured to be 0.9 hours. In contrast, the PeLEDs with subbandgap emission achieved  $T_{50}$  lifetimes at initial brightness of 4000, 6000, 8000, and

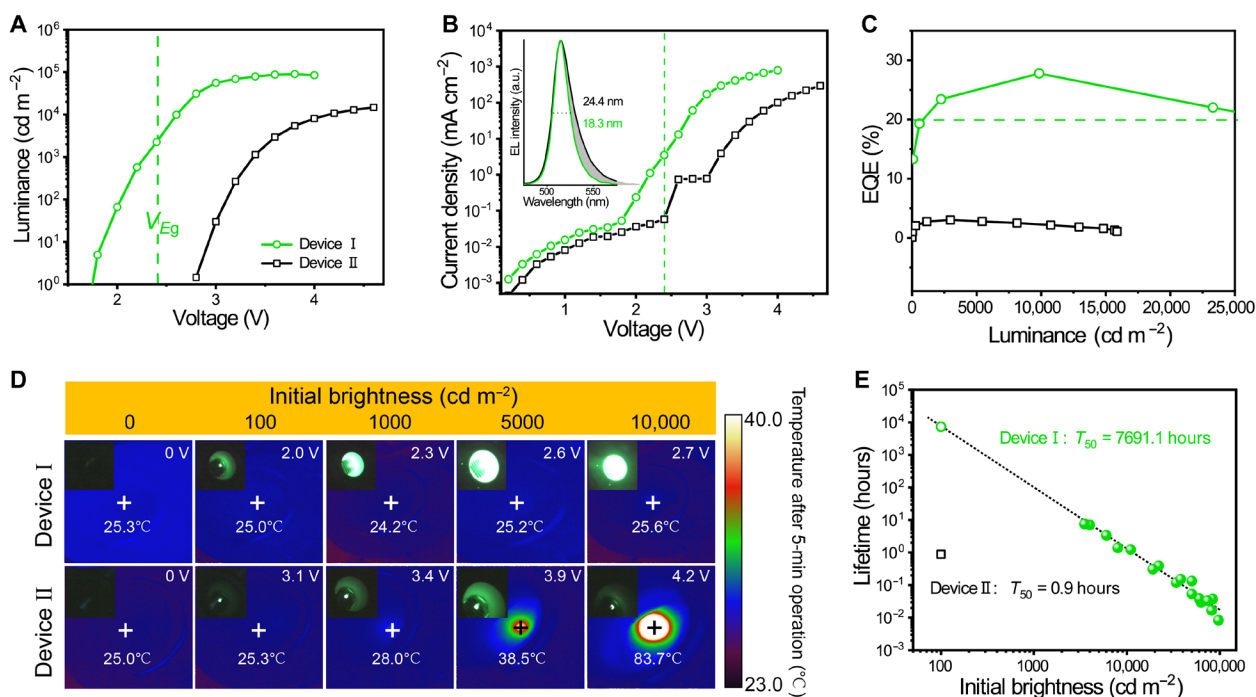


**Fig. 5. Comparison of device performance between subbandgap emissive PeLED (device I) and conventional PeLED (device II).** (A) Luminance-voltage ( $L$ - $V$ ) curves of device I and device II. (B) Current density-voltage ( $J$ - $V$ ) of device I and device II, with the inset showing the corresponding normalized EL spectra. (C) EQE-luminance curves of device I and device II. (D) The photographs and temperature of PeLEDs after 5 min of continuous operation at room temperature (25°C), which were measured by infrared thermography. (E) The  $T_{50}$  lifetime of device I and device II at different initial brightness levels.

11,000  $\text{cd m}^{-2}$  were directly measured to be 7.0, 3.2, 1.4, and 1.2 hours, respectively. The corresponding  $T_{50}$  lifetime at 100  $\text{cd m}^{-2}$  was estimated to be 7691.1 hours using the accelerated lifetime equation ( $L^n t = \text{constant}$ , where  $n$  is an acceleration factor, calculated to be 1.87 in this case). The corresponding brightness-time curves of PeLEDs operate at various initial brightness values as provided in fig. S21. The optimized lifetime was more than three orders of magnitudes higher than that of the control device. This demonstrates that the ultralow voltage-driven PeLED can effectively reduce Joule heat generation, offering valuable guidance for prolonging the operational lifetime of PeLEDs. In addition, the emission intensity of the PeLED is considerably influenced by the environmental temperature. For instance, when driven at a constant voltage of 2.3 V, the EL intensity shows a strong dependence on the ambient temperature. This observation suggests that the process involves thermal-assisted up-conversion EL phenomenon (fig. S22).

## DISCUSSION

In summary, we have demonstrated highly bright and efficient PeLEDs operating at ultralow driving voltages, achieved through collaborative optimizations of the emitter and adjacent CTLs. This encompassed effective suppression of interface recombination while maintaining excellent charge transport performance. As a result, under ultralow driving voltages (2.3 to 2.6 V), the PeLED achieved a high brightness range from 1000 to 10,000  $\text{cd m}^{-2}$  with elevated EQE levels (>20%). The Joule heat is nearly negligible under these low driving voltages, leading to a substantial enhancement in operational lifetime to 7691.1 hours. Our findings have revealed that the

utilization of low driving voltage holds the potential to considerably mitigate heat accumulation and bolster long-term operational stability. Moreover, the ultralow voltage-driven PeLEDs are anticipated to find applications in fascinating areas such as EL cooling, optical communications, and other energy applications.

## MATERIALS AND METHODS

### Materials

FABr (99.99%), PEABr (99.5%), poly-TPD, 1,3,5-tris(2-*N*-phenylbenzimidazolyl)-benzene, 18-crown-6, Me-4PACz (99%), (1,3,5-triazine-2,4,6-triyl)tris(benzene-3,1-diyl)tris(diphenylphosphine oxide), PO-T2T, and lithium fluoride (LiF) were purchased from Xi'an Yuri Solar Co. Ltd.  $\text{PbBr}_2$  (98%) was purchased from Tokyo Chemical Industry. CsBr (99.99%) was purchased from Alfa Aesar. PEDOT:PSS (Clevios P AI 4083) was purchased from Heraeus. PVP, dimethyl sulfoxide (99.9%), and CB (99.9%) were purchased from Sigma-Aldrich. All chemicals were used directly as received.

### Precursor solution fabrication

The perovskite precursor was prepared by dissolving FABr, PEABr, CsBr, and  $\text{PbBr}_2$  in dimethyl sulfoxide, maintaining a stoichiometric ratio of FABr:PEABr:CsBr: $\text{PbBr}_2 = x:0.35:1:1$  ( $x = 0$  to 0.3). The concentration of  $\text{PbBr}_2$  in the solution was maintained at 0.3 M. In addition, 18-crown-6 (6  $\text{mg ml}^{-1}$ ) was added to the precursor solution to suppress the crystallization of RP phases. Subsequently, the precursor solutions were stirred at 50°C overnight to ensure complete dissolution before being used for film deposition.

### Device fabrication and characterization

Patterned ITO substrates (7 to 9 ohms square<sup>-1</sup>, 20 mm by 20 mm; Advanced Election Technology Co. Ltd.) were cleaned through ultrasonication with successive immersions in detergent, deionized water, ethanol, and isopropanol. Subsequently, the cleaned substrates were purged with nitrogen gas (N<sub>2</sub>) and dried at 150°C to remove residual solvents. The cleaned substrates were placed inside a N<sub>2</sub>-filled glove box after UV-ozone treatment for 15 min. For devices using PEDOT:PSS as the HTL, the filtered PEDOT:PSS solution was spin-coated onto the substrate at 3000 rpm for 60 s, followed by annealing at 150°C for 15 min in ambient atmosphere. For devices using poly-TPD/Me-4PACz:PVP as HTLs, a solution of poly-TPD with a concentration of 4 mg ml<sup>-1</sup> (dissolved in CB) was spin-coated onto the substrate at 3000 rpm for 60 s and then annealed at 120°C for 15 min. Subsequently, a solution of Me-4PACz:PVP, with concentrations of 0.5/2 mg ml<sup>-1</sup> (dissolved in anhydrous ethanol), was spin-coated onto the substrate at 3000 rpm for 40 s. Subsequently, an annealing process was carried out at 120°C for a duration of 10 min. After cooling to room temperature, the perovskite thin film was prepared by spin-coating precursor solution at 5000 rpm for 40 s. Then, the as-deposited thin film was transferred into a petri dish that contains 100 μl of toluene for vapor-assisted crystallization treatment. Last, PO-T2T (20 nm) or TPBi (40 nm), LiF (1 nm), and Al electrodes (100 nm) were deposited through thermal evaporation within a high vacuum environment, maintaining a pressure of ~10<sup>-5</sup> Pa.

The EL spectra, *J-V-L* curves, EQE data, and device operational lifetime were measured using the Hamamatsu U6039-06 photonic measurement system. This comprehensive system consists of a computer-controlled Keithley 2400 source measure unit coupled with a fiber integration sphere and a photonic multichannel analyzer PMA-12. All of the device test processes were carried out in an N<sub>2</sub>-filled glove box. The surface temperature of PeLEDs under the continuous operation conditions were monitored by an infrared thermal camera (H16 Pro, HIKMICRO Sensing Technology).

### Film characterization

PL, time-resolved PL, and PLQY measurements were conducted using a spectrofluorometer (FLS1000, Edinburgh Instruments Ltd.) equipped with a 450-W xenon lamp, an optical laser with a wavelength of 375 nm, and a 15-cm integrating sphere for accurate measurements. The UV-visible absorption spectra were recorded using a Techcomp UV1101 II spectrophotometer. Atomic force microscopy measurements were performed using a Bruker Dimension Icon within a N<sub>2</sub>-filled glove box. The morphology and thickness of the emitter were captured using a field emission scanning electron microscopy (JSM-6700F, JEOL). The samples for TEM observation were prepared by peeling off the perovskite layer from the substrate into a CB solution and dropping it onto a copper mesh. Subsequently, TEM images were captured using a JEOL JEM-2010 electron microscope with an accelerating voltage of 200 kV. The chemical structure of emitter was subjected to further analysis through x-ray photoelectron spectroscopy and UV photoelectron spectroscopy using a VG Scientific ESCA Lab Mark II spectrometer, which was thoughtfully equipped with two ultrahigh vacuum chambers. XRD analysis was conducted to discern the perovskite phase structures of thin films prepared on glass substrates or zero-background holders. This analysis used a Rigaku SmartLab SE x-ray powder diffractometer operating at 40 kV with Cu Kα radiation (λ = 0.154 nm). GIWAXS measurements were performed on XEUSS SAXS/WAXS system. ToF-SIMS (ToF.SIMS 5,

IONTOF GmbH) was used to determine the ion distribution within the perovskite film. Oxygen ions were used as the sputtering ion source, and the sputtering area was 300 μm by 300 μm. The defects density is estimated using the equation  $N_t = \frac{2\epsilon\epsilon_0 V_{TFL}}{eL^2}$ , where ε<sub>0</sub> and ε represent the vacuum dielectric constant and relative dielectric constant, respectively. In the equation, *e* is the elementary charge, *L* is the thickness of emitter, and *V*<sub>TFL</sub> is determined by the intersection of the slopes in the ohmic and trap-filling limited regions.

### Calculation of the formation enthalpy

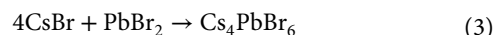
First-principles calculations of the formation enthalpy for each were performed within the density functional theory formalism, as implemented in Vienna Ab Initio Simulation Package (52, 53). The frozen-core projected augmented wave method with the generalized gradient approximation formulated by Perdew, Burke, and Ernzerhof as the exchange-correlation functionals was adopted to describe the electron-core interactions. The Brillouin zone for integrations in the reciprocal space was sampled using Monkhorst-Pack special *k*-point meshes (5 by 5 by 5 for 3D phase compounds). Moreover, in all computations, the electronic wave functions were expanded in a plane-wave basis with an energy cutoff of 520 eV, and cell parameters and atomic positions were fully relaxed until the energy and residual forces on atoms are converged to 1 × 10<sup>-6</sup> eV and declined to 0.01 eV Å<sup>-1</sup> by applying the conjugate-gradient algorithm, respectively. The formation enthalpy Δ*H*(*A<sub>m</sub>B<sub>n</sub>X<sub>l</sub>*) for a ternary phase *A<sub>m</sub>B<sub>n</sub>X<sub>l</sub>* is defined as the energy of the phase relative to the composition weighted average of the energies of the pristine constituents each in their stable configurations

$$\Delta H(A_m B_n X_l) = E(A_m B_n X_l) - mE(AX) - nE(BX_2) \quad (1)$$

where *E*(*A<sub>m</sub>B<sub>n</sub>X<sub>l</sub>*), *E*(*AX*), and *E*(*BX<sub>2</sub>*) are the energies of the final product compound *A<sub>m</sub>B<sub>n</sub>X<sub>l</sub>* and initial reactant compounds *AX* and *BX<sub>2</sub>*, all in their equilibrium geometries



$$\Delta H(\text{CsPbBr}_3) = -0.209 \text{ eV} (-20.1 \text{ kJ mol}^{-1})$$



$$\Delta H(\text{Cs}_4\text{PbBr}_6) = -0.689 \text{ eV} (-66.2 \text{ kJ mol}^{-1})$$



$$\Delta H(\text{Cs}_4\text{PbBr}_6) = -0.481 \text{ eV} (-46.2 \text{ kJ mol}^{-1})$$



$$\Delta H(\text{FAPbBr}_3) = -1.636 \text{ eV} (-157.1 \text{ kJ mol}^{-1})$$

## Supplementary Materials

This PDF file includes:

Figs. S1 to S22

Tables S1 and S2

References

## REFERENCES AND NOTES

- T.-H. Han, K. Y. Jang, Y. Dong, R. H. Friend, E. H. Sargent, T.-W. Lee, A roadmap for the commercialization of perovskite light emitters. *Nat. Rev. Mater.* **7**, 757–777 (2022).
- J. Jiang, M. Shi, Z. Xia, Y. Cheng, Z. Chu, W. Zhang, J. Li, Z. Yin, J. You, X. Zhang, Efficient pure-red perovskite light-emitting diodes with strong passivation via ultrasmall-sized molecules. *Sci. Adv.* **10**, eadn5683 (2024).
- L. N. Quan, B. P. Rand, R. H. Friend, S. G. Mhaisalkar, T.-W. Lee, E. H. Sargent, Perovskites for next-generation optical sources. *Chem. Rev.* **119**, 7444–7477 (2019).
- K. Lin, J. Xing, L. N. Quan, F. P. G. de Arquer, X. Gong, J. Lu, L. Xie, W. Zhao, D. Zhang, C. Yan, W. Li, X. Liu, Y. Lu, J. Kirman, E. H. Sargent, Q. Xiong, Z. Wei, Perovskite light-emitting diodes with external quantum efficiency exceeding 20 per cent. *Nature* **562**, 245–248 (2018).
- L. Kong, X. Zhang, Y. Li, H. Wang, Y. Jiang, S. Wang, M. You, C. Zhang, T. Zhang, S. V. Kershaw, W. Zheng, Y. Yang, Q. Lin, M. Yuan, A. L. Rogach, X. Yang, Smoothing the energy transfer pathway in quasi-2D perovskite films using methanesulfonate leads to highly efficient light-emitting devices. *Nat. Commun.* **12**, 1246 (2021).
- Y. B. Cao, D. Zhang, Q. Zhang, X. Qiu, Y. Zhou, S. Poddar, Y. Fu, Y. Zhu, J.-F. Liao, L. Shu, B. Ren, Y. Ding, B. Han, Z. He, D.-B. Kuang, K. Wang, H. Zeng, Z. Fan, High-efficiency, flexible and large-area red/green/blue all-inorganic metal halide perovskite quantum wires-based light-emitting diodes. *Nat. Commun.* **14**, 4611 (2023).
- Y. Fong, H. Li, M. Zhu, Y. Gao, Q. Cai, G. Lu, X. Dai, Z. Ye, H. He, Nucleophilic reaction-enabled chloride modification on CsPbI<sub>3</sub> quantum dots for pure red light-emitting diodes with efficiency exceeding 26%. *Angew. Chem. Int. Ed. Engl.* **63**, 202318777 (2024).
- W. Bai, T. Xuan, H. Zhao, H. Dong, X. Cheng, L. Wang, R.-J. Xie, Perovskite light-emitting diodes with an external quantum efficiency exceeding 30%. *Adv. Mater.* **35**, e2302283 (2023).
- S. Yuan, L. Dai, Y. Sun, F. Auras, Y.-H. Zhou, R.-Z. An, Y. Liu, C. Ding, C. Cassidy, X. Tang, S.-C. Dong, H.-B. Kang, K. Chen, X. Liu, Z.-F. Ye, Y. Zhao, C. Adachi, L.-S. Liao, N. C. Greenham, Y. Qi, S. D. Stranks, L.-S. Cui, R. H. Friend, Efficient blue electroluminescence from reduced-dimensional perovskites. *Nat. Photonics* **18**, 425–431 (2024).
- N. Li, K. Han, W. Spratt, S. Bedell, J. Ott, M. Hopstaken, F. Libsch, Q. Li, D. Sadana, Ultra-low-power sub-photon-voltage high-efficiency light-emitting diodes. *Nat. Photonics* **13**, 588–592 (2019).
- D. Di, A. S. Romanov, L. Yang, J. M. Richter, J. P. H. Rivett, S. Jones, T. H. Thomas, M. Abdi Jalebi, R. H. Friend, M. Linnolahti, M. Bochmann, D. Credgington, High-performance light-emitting diodes based on carbene-metal-amides. *Science* **356**, 159–163 (2017).
- P. Gao, Y. Zhang, P. Qi, S. Chen, Efficient InP Green quantum-dot light-emitting diodes based on organic electron transport layer. *Adv. Opt. Mater.* **10**, 2202066 (2022).
- Y. Lian, D. Lan, S. Xing, B. Guo, Z. Ren, R. Lai, C. Zou, B. Zhao, R. H. Friend, D. Di, Ultralow-voltage operation of light-emitting diodes. *Nat. Commun.* **13**, 3845 (2022).
- Y. Gao, B. Li, X. Liu, H. Shen, Y. Song, J. Song, Z. Yan, X. Yan, Y. Chong, R. Yao, S. Wang, L. S. Li, F. Fan, Z. Du, Minimizing heat generation in quantum dot light-emitting diodes by increasing quasi-fermi-level splitting. *Nat. Nanotechnol.* **18**, 1168–1174 (2023).
- Q. Su, S. Chen, Thermal assisted up-conversion electroluminescence in quantum dot light emitting diodes. *Nat. Commun.* **13**, 369 (2022).
- T. Sadi, I. Radevici, J. Oksanen, Thermophotonic cooling with light-emitting diodes. *Nat. Photonics* **14**, 205–214 (2020).
- N. Li, Y. Jia, Y. Guo, N. Zhao, Ion migration in perovskite light-emitting diodes: Mechanism, characterizations, and material and device engineering. *Adv. Mater.* **34**, e2108102 (2022).
- L. Zhao, K. Roh, S. Kacmoli, K. Al Kurdi, S. Jhulki, S. Barlow, S. R. Marder, C. Gmachl, B. P. Rand, Thermal management enables bright and stable perovskite light-emitting diodes. *Adv. Mater.* **32**, e2000752 (2020).
- L. Zhao, K. M. Lee, K. Roh, S. U. Z. Khan, B. P. Rand, Improved outcoupling efficiency and stability of perovskite light-emitting diodes using thin emitting layers. *Adv. Mater.* **31**, e1805836 (2019).
- C. Zou, Y. Liu, D. S. Ginger, L. Y. Lin, Suppressing efficiency roll-off at high current densities for ultra-bright green perovskite light-emitting diodes. *ACS Nano* **14**, 6076–6086 (2020).
- D. Ma, K. Lin, Y. Dong, H. Choubisa, A. H. Proppe, D. Wu, Y.-K. Wang, B. Chen, P. Li, J. Z. Fan, F. Yuan, A. Johnston, Y. Liu, Y. Kang, Z.-H. Lu, Z. Wei, E. H. Sargent, Distribution control enables efficient reduced-dimensional perovskite LEDs. *Nature* **599**, 594–598 (2021).
- Z. Liu, W. Qiu, X. Peng, G. Sun, X. Liu, D. Liu, Z. Li, F. He, C. Shen, Q. Gu, F. Ma, H.-L. Yip, L. Hou, Z. Qi, S.-J. Su, Perovskite light-emitting diodes with EQE exceeding 28% through a synergetic dual-additive strategy for defect passivation and nanostructure regulation. *Adv. Mater.* **33**, e2103268 (2021).
- L. N. Quan, R. Quintero-Bermudez, O. Voznyy, G. Walters, A. Jain, J. Z. Fan, X. Zheng, Z. Yang, E. H. Sargent, Highly emissive green perovskite nanocrystals in a solid state crystalline matrix. *Adv. Mater.* **29**, 1605945 (2017).
- Y. Jiang, C. Sun, J. Xu, S. Li, M. Cui, X. Fu, Y. Liu, Y. Liu, H. Wan, K. Wei, T. Zhou, W. Zhang, Y. Yang, J. Yang, C. Qin, S. Gao, J. Pan, Y. Liu, S. Hoogland, E. H. Sargent, J. Chen, M. Yuan, Synthesis-on-substrate of quantum dot solids. *Nature* **612**, 679–684 (2022).
- K. Lin, C. Yan, R. P. Sabatini, W. Feng, J. Lu, K. Liu, D. Ma, Y. Shen, Y. Zhao, M. Li, C. Tian, L. Xie, E. H. Sargent, Z. Wei, Dual-phase regulation for high-efficiency perovskite light-emitting diodes. *Adv. Funct. Mater.* **32**, 2200350 (2022).
- X. Chen, F. Zhang, Y. Ge, L. Shi, S. Huang, J. Tang, Z. Lv, L. Zhang, B. Zou, H. Zhong, Centimeter-sized Cs<sub>5</sub>PbBr<sub>6</sub> crystals with embedded CsPbBr<sub>3</sub> nanocrystals showing superior photoluminescence: Nonstoichiometry induced transformation and light-emitting applications. *Adv. Funct. Mater.* **28**, 1706567 (2018).
- Y. Ke, J. Guo, D. Kong, J. Wang, G. Kusch, C. Lin, D. Liu, Z. Kuang, D. Qian, F. Zhou, G. Zhang, M. Niu, Y. Cao, R. A. Oliver, D. Dai, Y. Jin, N. Wang, W. Huang, J. Wang, Efficient and bright deep-red light-emitting diodes based on a lateral 0D/3D perovskite heterostructure. *Adv. Mater.* **36**, e2207301 (2024).
- L. Zhuang, L. Zhai, Y. Li, H. Ren, M. Li, S. P. Lau, Mixed dimensional 0D/3D perovskite heterostructure for efficient green light-emitting diodes. *J. Mater. Chem. C* **9**, 14318–14326 (2021).
- K.-Y. Baek, W. Lee, J. Lee, J. Kim, H. Ahn, J. I. Kim, J. Kim, H. Lim, J. Shin, Y.-J. Ko, H.-D. Lee, R. H. Friend, T.-W. Lee, J. Lee, K. Kang, T. Lee, Mechanochemistry-driven engineering of 0D/3D heterostructure for designing highly luminescent Cs–Pb–Br perovskites. *Nat. Commun.* **13**, 4263 (2022).
- D. R. Cerretti, A. Zohar, R. Kozlov, H. Dong, G. Uraltsev, O. Girshevitz, I. Pinkas, L. Avram, G. Hodes, D. Cahen, Eppur si muove: Proton diffusion in halide perovskite single crystals. *Adv. Mater.* **32**, e2002467 (2020).
- Y. Ren, J. Hua, Z. Han, M. Sun, S. Lü, Brightly luminescent green-emitting halide perovskite light emitting diode by employing the whole single crystal. *Chem. Eng. J.* **452**, 139160 (2023).
- C. Bao, X. Peng, L. Ying, Y. Mei, B. Zhang, H. Long, Investigation of CsPbBr<sub>3</sub> CVD dynamics at various temperatures. *Phys. Chem. Chem. Phys.* **23**, 23214–23218 (2021).
- T. Xiang, T. Li, M. Wang, W. Zhang, M. Ahmadi, X. Wu, T. Xu, M. Xiao, L. Xu, P. Chen, 12-Crown-4 ether assisted in-situ grown perovskite crystals for ambient stable light emitting diodes. *Nano Energy* **95**, 107000 (2022).
- L. N. Quan, Y. Zhao, F. P. García de Arquer, R. Sabatini, G. Walters, O. Voznyy, R. Comin, Y. Li, J. Z. Fan, H. Tan, J. Pan, M. Yuan, O. M. Bakr, Z. Lu, D. H. Kim, E. H. Sargent, Tailoring the energy landscape in quasi-2D halide perovskites enables efficient green-light emission. *Nano Lett.* **17**, 3701–3709 (2017).
- C. Rodà, M. Fasoli, M. L. Zaffalon, F. Cova, V. Pinchetti, J. Shamsi, A. L. Abdelhady, M. Imran, F. Meinardi, L. Manna, A. Vedda, S. Brovelli, Understanding thermal and a-thermal trapping processes in lead halide perovskites towards effective radiation detection schemes. *Adv. Funct. Mater.* **31**, 2104879 (2021).
- X. Lao, Z. Yang, Z. Su, Z. Wang, H. Ye, M. Wang, X. Yao, S. Xu, Luminescence and thermal behaviors of free and trapped excitons in cesium lead halide perovskite nanosheets. *Nanoscale* **10**, 9949–9956 (2018).
- M. Dendebera, Y. Chornodolskyy, R. Gamernyk, O. Antonyak, I. Pashuk, S. Myagkota, I. Gniliitskiy, V. Pankratov, V. Vistovskyy, V. Mykhaylyk, M. Grinberg, A. Voloshinovskii, Time resolved luminescence spectroscopy of CsPbBr<sub>3</sub> single crystal. *JOL* **225**, 117346 (2020).
- J. S. Kim, J.-M. Heo, G.-S. Park, S.-J. Woo, C. Cho, H. J. Yun, D.-H. Kim, J. Park, S.-C. Lee, S.-H. Park, E. Yoon, N. C. Greenham, T.-W. Lee, Ultra-bright, efficient and stable perovskite light-emitting diodes. *Nature* **611**, 688–694 (2022).
- Y. Jiang, M. Cui, S. Li, C. Sun, Y. Huang, J. Wei, L. Zhang, M. Lv, C. Qin, Y. Liu, M. Yuan, Reducing the impact of auger recombination in quasi-2D perovskite light-emitting diodes. *Nat. Commun.* **12**, 336 (2021).
- A. Al-Ashouri, E. Köhnen, B. Li, A. Magomedov, H. Hempel, P. Caprioglio, J. A. Márquez, A. B. Morales Vilches, E. Kasparavicius, J. A. Smith, N. Phung, D. Menzel, M. Grischek, L. Kegelman, D. Skroblin, C. Gollwitzer, T. Malinauskas, M. Jošt, G. Matič, B. Rech, R. Schlattmann, M. Topič, L. Korte, A. Abate, B. Stannowski, D. Neher, M. Stollerfoht, T. Unold, V. Getautis, S. Albrecht, Monolithic perovskite/silicon tandem solar cell with >29% efficiency by enhanced hole extraction. *Science* **370**, 1300–1309 (2020).
- W. Xiong, C. Zou, W. Tang, S. Xing, Z. Wang, B. Zhao, D. Di, Efficient and bright blue perovskite LEDs enabled by a carbazole-phosphonic acid interface. *ACS Energy Lett.* **8**, 2897–2903 (2023).
- Z. Li, Z. Chen, Z. Shi, G. Zou, L. Chu, X.-K. Chen, C. Zhang, S. K. So, H.-L. Yip, Charge injection engineering at organic/inorganic heterointerfaces for high-efficiency and fast-response perovskite light-emitting diodes. *Nat. Commun.* **14**, 6441 (2023).
- Z. Wang, F. Yuan, W. Sun, H. Shi, T. Hayat, A. Alsaedi, L. Fan, Z. Tan, Multifunctional p-type carbon quantum dots: A novel hole injection layer for high-performance perovskite light-emitting diodes with significantly enhanced stability. *Adv. Opt. Mater.* **7**, 1901299 (2019).

44. Z. Wang, Z. Luo, C. Zhao, Q. Guo, Y. Wang, F. Wang, X. Bian, A. Alsaedi, T. Hayat, Z. Tan, Efficient and stable pure green all-inorganic perovskite CsPbBr<sub>3</sub> light-emitting diodes with a solution-processed NiO<sub>x</sub> interlayer. *J. Phys. Chem. C* **121**, 28132–28138 (2017).
45. Y. Zhao, W. Feng, M. Li, J. Lu, X. Qin, K. Lin, J. Luo, W.-H. Zhang, E. L. Lim, Z. Wei, Efficient perovskite light-emitting diodes with chemically bonded contact and regulated charge behavior. *Nano Lett.* **23**, 8560–8567 (2023).
46. Y.-C. Ye, Y. Shen, W. Zhou, S.-C. Feng, J.-Y. Wang, Y.-Q. Li, J.-X. Tang, Interfacial molecule control enables efficient perovskite light-emitting diodes. *Adv. Funct. Mater.* **33**, 2307818 (2023).
47. J. Wang, C. Song, Z. He, C. Mai, G. Xie, L. Mu, Y. Cun, J. Li, J. Wang, J. Peng, Y. Cao, All-solution-processed pure formamidinium-based perovskite light-emitting diodes. *Adv. Mater.* **30**, e1804137 (2018).
48. L. Meng, E.-P. Yao, Z. Hong, H. Chen, P. Sun, Z. Yang, G. Li, Y. Yang, Pure formamidinium-based perovskite light-emitting diodes with high efficiency and low driving voltage. *Adv. Mater.* **29**, 1603826 (2017).
49. R. Zhu, Z. Luo, H. Chen, Y. Dong, S.-T. Wu, Realizing Rec. 2020 color gamut with quantum dot displays. *Opt. Express* **23**, 23680–23693 (2015).
50. X. Shen, X. Zhang, Z. Wang, X. Gao, Y. Wang, P. Lu, X. Bai, J. Hu, Z. Shi, W. W. Yu, Y. Zhang, Bright and efficient pure red perovskite nanocrystals light-emitting devices via in situ modification. *Adv. Funct. Mater.* **32**, 2110048 (2022).
51. R. Zeng, L. Zhu, M. Zhang, W. Zhong, G. Zhou, J. Zhuang, T. Hao, Z. Zhou, L. Zhou, N. Hartmann, X. Xue, H. Jing, F. Han, Y. Bai, H. Wu, Z. Tang, Y. Zou, H. Zhu, C.-C. Chen, Y. Zhang, F. Liu, All-polymer organic solar cells with nano-to-micron hierarchical morphology and large light receiving angle. *Nat. Commun.* **14**, 4148 (2023).
52. G. Kresse, J. Furthmüller, Efficiency of Ab-Initio total energy calculations for metals and semiconductors using a plane-wave basis set. *Comput. Mater. Sci.* **6**, 15–50 (1996).
53. G. Kresse, J. Furthmüller, Efficient iterative schemes for ab initio total-energy calculations using a plane-wave basis set. *Phys. Rev. B* **54**, 11169–11186 (1996).
54. X. Chen, Y. Wang, J. Song, X. Li, J. X. H. Zeng, H. Sun, Temperature dependent reflectance and ellipsometry studies on a CsPbBr<sub>3</sub> single crystal. *J. Phys. Chem. C* **123**, 10564–10570 (2019).

#### Acknowledgments

**Funding:** This research was supported by the National Natural Science Foundation of China (52102159, 52272141, 51972060, 12074068, 22103013, and 22302012), the Natural Science Foundation of Fujian Province (2021 J01187, 2020 J02017, 2021 J06021, 2021 J01184, and 2020 J01931), National Key Research and Development Program of China (2023YFB3611800), and National Science Fund for Excellent Young Scholars (Overseas). **Author contributions:** Conceptualization: S.Z., Z.W., L.Z., and F.Y. Methodology: S.Z., Z.W., F.H., L.L., and F.Y. Software: S.Z. and L.L. Validation: S.Z., Z.W., N.J., H.H., X.W., T.P., F.H., F.Y., and D.C. Formal analysis: S.Z., Z.W., L.Z., T.W., and D.C. Investigation: S.Z., Z.W., N.J., H.H., X.W., D.L., L.L., F.Y., and D.C. Resources: Z.W., F.H., R.Z., and D.C. Data curation: S.Z., Z.W., and F.Y. Writing—original draft: S.Z., Z.W., D.L., L.Z., T.W., and F.Y. Writing—review and editing: Z.W., X.W., D.L., T.P., L.Z., R.Z., L.L., F.Y., and D.C. Visualization: S.Z., Z.W., Q.T., Jinyang L., C.L., Jinsui L., and F.Y. Supervision: Z.W., R.Z., F.Y., and D.C. Project administration: Z.W., F.Y., and D.C. Funding acquisition: Z.W., F.H., F.Y., and D.C. **Competing interests:** The authors declare that they have no competing interests. **Data and materials availability:** All data needed to evaluate the conclusions in the paper are present in the paper and/or the Supplementary Materials.

Submitted 15 April 2024

Accepted 1 August 2024

Published 6 September 2024

10.1126/sciadv.adp8473